Feasibility study of an induction motor rim drive for an aircraft boundary-layer-ingestion fan

Alexander C. Smith, Matteo F. Iacchetti, Paul M. Tuohy

School of Electrical and Electronic Engineering, the University of Manchester, UK
Sandy.Smith@manchester.ac.uk, matteo.iacchetti@manchester.ac.uk, paul.tuohy-2@manchester.ac.uk

Keywords: Induction motor, rim drive, centrifugal stress, boundary layer ingestion.

Abstract

This paper presents a feasibility study for an induction motor rim drive to power aircraft BLI fans. The design is developed from a BLI-fan specification for traditional aircraft architecture: the rotor is fastened to the rim of the blade shroud, not to obstruct the fan duct and interfere with the air-flow. The main objective of this study is the identification of achievable power density and efficiency levels with an induction motor rim drive configuration considering the structural requirements for the integrity of the rotor operating with high tip speeds. The proposed 250 kW, 14,000 rpm design example achieves an efficiency in excess of 97% with an active mass around 20 kg.

1 Introduction

Concerns about air pollution along with the rapid growth in air traffic have set challenging targets for the next generations of aircraft to reduce emissions, fuel consumption and noise [1]. Boundary layer ingestion (BLI) which reduces drag on the aircraft, is implemented through an array of electrically-driven fans. BLI has been identified as potentially beneficial towards achieving these targets, without necessarily requiring disruptive changes in the aircraft architecture [2]. BLI however is one of the key concepts which will allow radically different layouts based on distributed propulsion architectures that brings significant advantages in terms of noise and fuel consumption reduction [3-5]. This paper presents a feasibility study for an electrical rim drive to power BLI fans. The design is developed from a typical BLI fan specification for traditional aircraft 'tube-and-wing' architectures: the rotor is housed on the rim of the fan shroud so that it does not obstruct the fan duct and interfere with the air-flow. A similar rim-drive layout concept has been already successfully implemented in marine thrusters [5]. Induction motor technology is adopted because of some key features such as no cogging torque, easy assembly, potentially no need for power electronics if operating at roughly constant speed, and the possibility to reduce weight using an aluminium cage. These features all align closely with the needs of a high-speed fan drive. The main objective of this study is the identification of achievable power density and efficiency levels with the rim drive configuration, having in mind the structural requirements due to the high peripheral speed resulting from the rim configuration. In that respect, the paper explores the different options of aluminium and fabricated copper cages.
Section 2 presents the electromagnetic designs based on classical sizing equations and steady-state FE analyses. The stress analysis of the rotor candidates is described in Section 3 and Section 4 draws conclusions.

2 Electromagnetic design

2.1 Specifications

The concept of a rim drive is illustrated for a fan in Fig. 1.

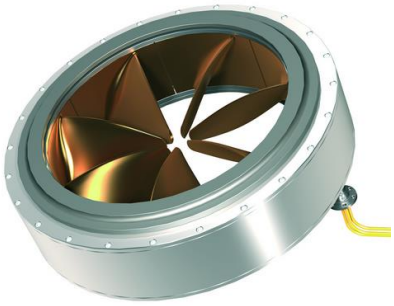

Figure 1: Layout of a rim drive for a fan (from Schottel [7])

The BLI fan specification shown in Table 1 was used in this paper: the rotor core is mounted on the blade shroud but is mechanically designed not to rely on any stiffness and retention capability of the blades and shroud. In a rim drive topology, the mechanical airgap length should be compatible with the clearance usually adopted between the blade shroud and duct. The airgap length in the baseline design is set to the relatively large value of 2 mm which is a pessimistic design value in terms of the magnetising current of an IM.

Duct diameter	mm	300
Rotational speed	rpm	14,000
Max fundamental frequency	Hz	1400
Rated power	kW	250

Table 1: Design specifications

2.1 Sizing approach

In PM machines, a common practice to minimise the mass is to adopt a high pole number p so as to reduce the depth of the back iron in the stator and rotor cores. The limitation for the pole number comes from the maximum allowed fundamental

frequency and the need to keep iron losses below a reasonable value. In an IM however, limiting the magnetising current is another design factor which needs to be considered in the choice of the pole number. A high magnetising current and low power factor are both detrimental to efficiency and the power ratings of the converter.

To determine the optimal pole number as well as the leading dimensions of the core (rotor outer diameter d_{re} and stack length L_{stack}), a preliminary parametric analysis has been undertaken using well-known sizing equations [8] and considering a fixed inner rotor diameter d_{re} = 310 mm.

Using the relationship between the flux densities in the airgap and rotor back iron B_g and B_{ry} as follows:

$$B_{ry} h_{ry} k_{stak} = \frac{2}{\pi} \tau B_g \quad , \quad \tau = \frac{\pi d_{ro}}{p} \tag{1}$$

and assuming a rotor slot depth to rotor back iron depth ratio $\xi_r \approx 0.5$ (for round rotor bars), the required rotor outer diameter d_{ro} can be expressed as a function of p

$$d_{ro} = d_{ri} + 2\left(1 + \xi_r h_{ry}\right) \quad \Rightarrow \quad d_{ro} = \frac{d_{ri}}{1 - 2\xi_r \frac{B_g}{B_{ry}} \frac{1}{p}} \tag{2}$$

The resulting stator outer diameter can be derived using the same approach: accounting for the airgap, the stator back iron and slot depths with a suitable stator slot to back iron depth ratio $\xi_s \approx 1.0$ and stator back iron flux density B_{sy}

$$d_{so} = d_{ro}\left(1 + 2(1 + \xi_s)\frac{B_g}{B_{sy}}\frac{1}{p}\right) + 2g \tag{3}$$

For a given airgap flux density B_g , airgap length g, diameter d_{ro} and pole number p, the required magnetising linear current density A_μ is given by [8]

$$A_\mu = \frac{k_c}{\sqrt{2}\mu_0 k_w} B_g p \frac{g}{d_{ro}} \tag{4}$$

where k_c is the airgap Carter factor. *A is* the total linear current density, so that the power factor can be expressed as

$$PF = \sqrt{A^2 - {A_\mu}^2}\,/A \tag{5}$$

The sizing equation for the mechanical power written in terms of the leading dimensions, the airgap field, and the active linear current density $PF{\cdot}A$ is

$$P = \frac{\pi^2}{\sqrt{2}} k_w n B_g \eta \; PF \; A \; {d_{ro}}^2 l_{stack} \tag{6}$$

Once l_{stack} is found from (6) for the required mechanical power and assumed flux density and linear current density, the core volume can be calculated as

$$V_{core} = \frac{\pi}{4}\left({d_{so}}^2 - {d_{ri}}^2\right) l_{stack} \tag{7}$$

with the ratio PF/V_{core} estimated from (5) and (7). The model can be further refined to estimate the total active mass of the machine, including core, stator winding and rotor cage.

Figure 2 reports the rotor outer diameter, power factor, stack length and ratio PF/V_{core} as a function of pole number p for three values of linear current density A within the range 55-75 kA/m. These curves were obtained assuming the following values for the ancillary parameters B_g=1T, B_{sy}=2T, B_{ry}=1.8T (appropriate for cobalt-iron Vacoflux 50 and VacodurS+ for the stator and rotor laminations respectively), ξ_s=1, ξ_r=0.5, k_c=1.1 (compatible with the relatively large airgap length).

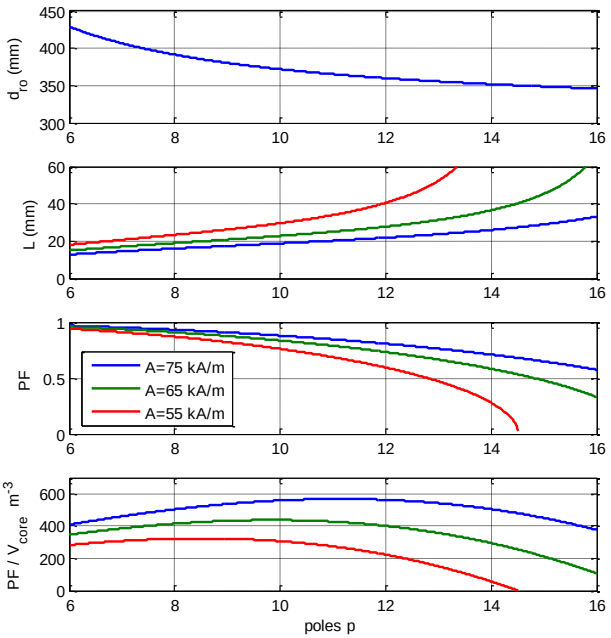

Figure 2: Trends for rotor outer diameter d_{ro}, stack length l_{stack}, power factor PF, and PF to core volume V_{core} ratio as a function of pole number and linear current density A.

The trend for the PF to core volume ratio in Fig. 2 shows that the optimal pole number grows with the stator linear current density and peaks around p=10 for a linear current density of 65 kA/m. The slightly higher pole number p=12 was eventually chosen to bring further reduction in the overall mass, at the expense of higher iron losses, because it reduces the end winding length although the simplified analysis does not capture this aspect. A more refined analysis considering the power density and conducted for the case p=12 identified the optimal (electric loading) around 65 kA/m, as shown in Fig. 3, corresponding to a required axial length l_{stack}=33mm and an estimated base efficiency slightly above 97% (Fig. 4)

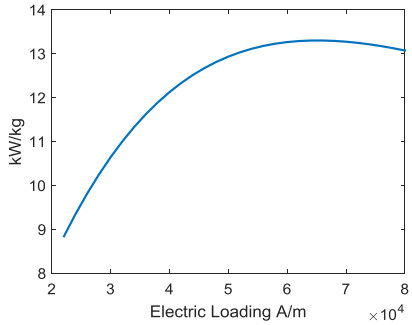

Figure 3: Power density (active mass) versus electric loading

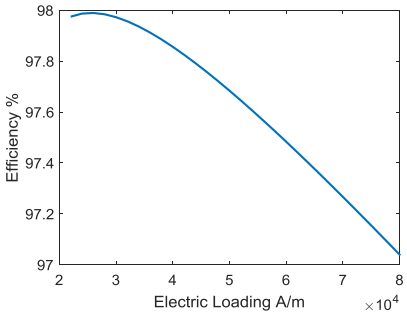

Figure 4: Estimated efficiency versus electric loading (only Joule and iron losses based on simplified calculations)

2.2 Final design

The final design for p=12 poles was carried out using an iterative optimisation based on 2D FE analyses of the IM operating points at steady state (time-harmonic formulation with rotor conductivity corrected by the slip), including appropriate corrections for the 3D effects (end-windings and rotor ring). The efficiency accounts for stator and rotor Joule losses and iron losses, and includes also windage losses [8]. Iron losses are calculated by using lamination datasheets [9] and accurate peak flux densities from the FE analysis. Data for 0.1 mm cobalt iron laminations were not directly available and were estimated by scaling up the eddy-current loss component for 0.35mm laminations by a factor 2.5 following the behaviour of similar materials with available data for both thicknesses [10]. The windage losses were estimated from:

$$P_{lw} = \frac{1}{32} C_M \pi \varrho \omega^3 {d_{ro}}^4 l_{stack} \quad , \; C_M = 0.065 \frac{(2g/d_{ro})^{0.3}}{{Re_g}^{0.2}} \qquad (8)$$

where Re_g is the value of the Reynolds number for the Couette flow in the airgap and ρ is the air density.

The main geometric and electric data for the main result – referred to as "design A", are given in Table 2: aluminium was chosen for the rotor cage initially to save mass and reduce centrifugal stresses in the rotor. Table 3 details the loss break down for the baseline design. The design of the cooling system is not included at this stage, but it is worth noticing that during flight the external air is at a very low temperature (-50°C) and makes the use of direct air cooling possible to cope with the high electric loading.

Inner, outer stator diameter	mm	410 , 358
Inner, outer rotor diameter	mm	354 , 305
Stator, rotor slot number	-	72 , 77
Stator, rotor slot area	-	152 , 73
Rotor bar diameter	mm	9.6
Core stack length	mm	33
Airgap length	mm	2
Electric loading A	kA/m	65
Surface current density (stator)	A/mm^2	13
Rated stator voltage (ph), current	V, A	240 , 515
Rated slip	%	0.76
Rated power factor	-	0.69
Rated efficiency	%	96.3

Table 2: Geometric and electric data (design A).

Stator Joule losses	kW	2.79
Rotor Joule losses	kW	1.93
Iron losses	kW	4.19
Windage losses	kW	0.70

Table 3: Losses breakdown (design A).

Figure 5 shows the flux density distribution at rated load (250 kW) for the main design (A) and the details of the magnetic structur.To explore the impact of the rotor cage material, four alternative designs based on the same magnetic structure were investigated but with different materials in the stator core and rotor cage, as shown in Table 3.

design	cage	Stator lamination thickness (mm)	mass (kg)	rated PF	rated eff. %
A	Al	0.35	19.0	0.69	96.3
B	Cu	0.35	20.9	0.68	96.5
C	Al	0.10	19.0	0.69	97.2
D	Cu	0.10	20.9	0.68	97.4

Table 3: Mass, power factor and efficiency for different designs

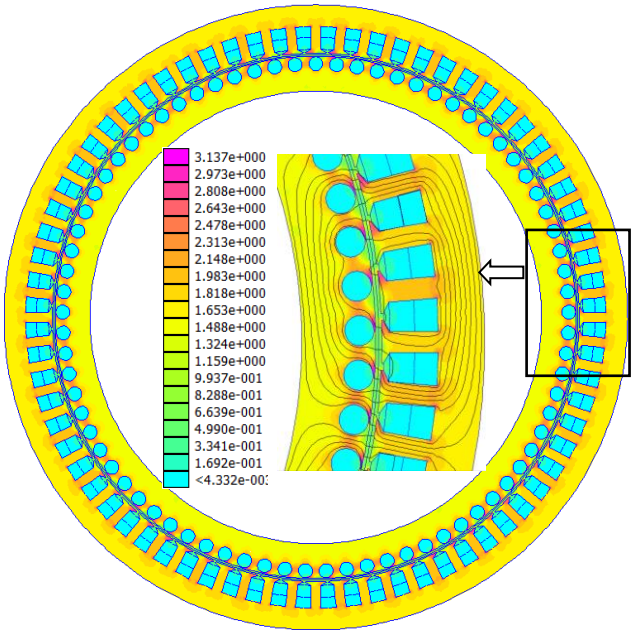

Figure 5: IM core structure and flux density (T) distribution at rated load for design A

Figure 6 shows the torque, current, power factor and efficiency versus slip characteristics of designs A and B. The efficiency curves in the useful slip range for all the designs are shown in Fig. 7 along with the mechanical power: iron losses occur mainly in the stator core and for this reason they are simply added to the input power and do not impact on the output power characteristics. This explains why designs C and D have the same characteristics as A and B respectively. All the designs have the rated operating point (P_{mech}=250 kW) close to the maximum efficiency point. The efficiency curves

show that despite the promising results of Fig. 4 (based on simplified calculations), efficiency values in excess of 97% can only be achieved using 0.10 mm laminations for the stator core because the high stator frequency makes iron losses more important than the Joule losses in the stator and rotor. A copper cage provides an extra 0.2-0.3% efficiency gain compared to aluminium, but it increases the mass by 10% and increases the centrifugal stresses in the rotor, as shown in Section 3.

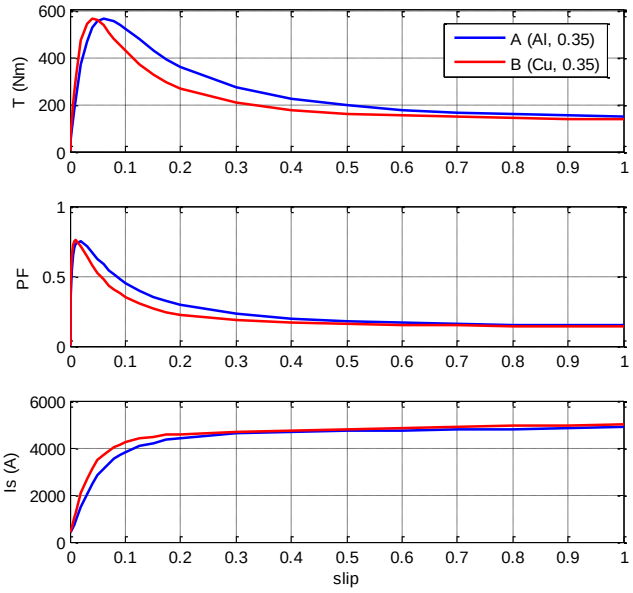

Figure 6: Torque, power factor and stator current characteristics of thedifferent designs

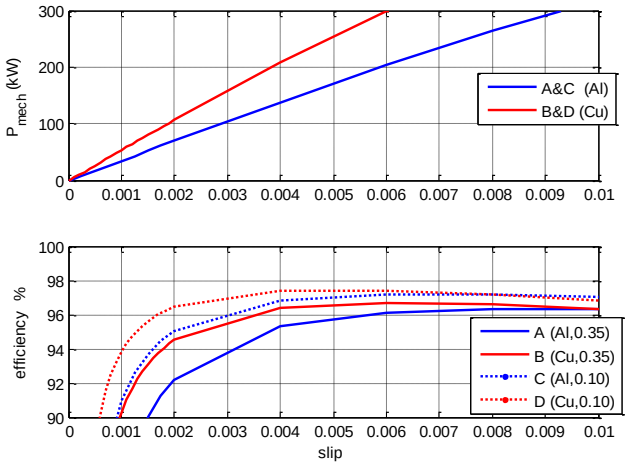

Figure 7: Mechanical power and efficiency characteristics at low slip for the different designs.

3 Mechanical design

The rotor tip speed in this machine is about 260 m/s, which would make a solid steel rotor recommended [11]. The rim drive topology however has a very low aspect ratio l_{stack}/d_s making the inherently low axial bending stiffness of a laminated stack not particularly critical. Linear elastic FE analyses were used to assess the rotor strength: the rotor symmetry enabled a small section corresponding to a bar pitch and half the stack length to be analysed instead of the full rotor. Slider boundary conditions were imposed at the section cuts as shown in Fig. 8.

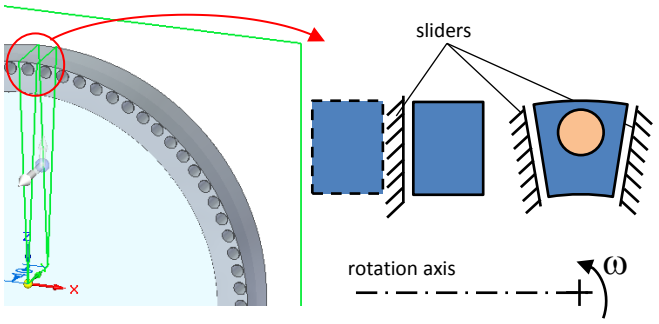

Figure 8: Rotor section and boundary conditions for the mechanical analysis.

Figure 9 presents the Von Mises stress map for the rotor with an aluminium cage and a non-supported end ring, to assess the worst case scenario. Although the peak Von Mises stress in the core near the inner surface (635 MPa) is below the yield stress of VacodurS+ (800 MPa), the aluminium ring is overstressed (peak Von Mises stress 239 MPa) and would fail (Al 6063 yield stress = 135 MPa). The thin slot bridge also experiences a local stress concentration which brings the Von Mises stress (1100 MPa) well above the yield value, making the stress distribution in the thin bridge unrealistic. The real distribution should be assessed with an elasto-plastic analysis, but the stress concentration can be relieved simply by flattening the top of the bar.

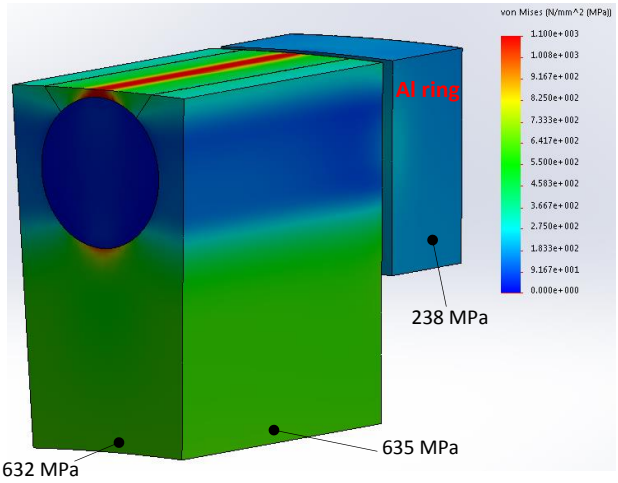

Figure 9: Von Mises stress distribution with free ring (Al).

Figure 10 shows an improved design adopting flattened bars and a supporting end ring can which is shrunk-fit onto the aluminium ring. The can is made of high tensile stress steel (900 MPa yield stress) but it could also be made of carbon fibre composite for example, which would be lighter. The shrink fit is designed to generate an interface pressure of around 20 MPa. The Von Mises stress in the aluminium ring

is considerably reduced and the ring is capped while the supporting can is fully in the elastic region, and there is no longer significant stress concentration in the slot bridge.
The geometry of the supporting can and shrink fit may be optimised further in order to keep the stress in the aluminium ring fully below the yield value.

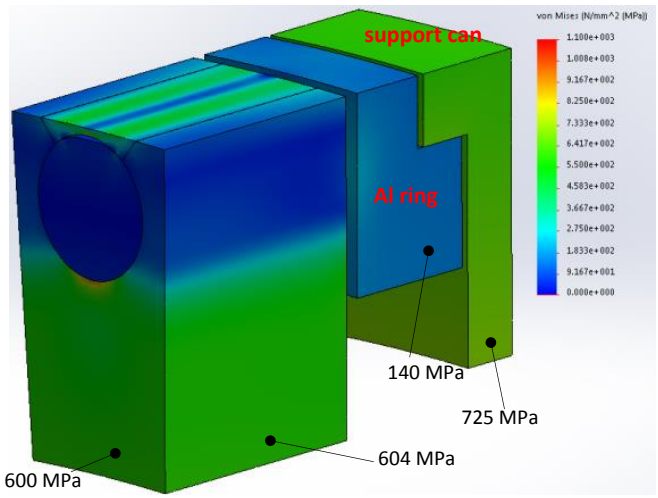

Figure 10: Von Mises stress distribution in the improved design with support bandage can.

Finally, the stress distribution in case of using copper instead of aluminium for the rotor cage one was analysed. As copper is more than 3 times heavier than aluminium, it results in an increase of the centrifugal stresses in the iron core and on the requirements for the bandage can, which are not well repaid by the extra 0.2-0.4% efficiency gain. The centrifugal stress in the rotor core, in particular, become close to the yield stress of VacodurS+, whereas the bandage can provides stress relief mainly in the short circuit ring. This would imply the need of extra bandage on the rotor core, which is difficult to fit within the small mechanical airgap. Some improvement may be achieved by optimising the rotor bar geometry, but yet again the benefits in terms of improved efficiency are not worth the effort. In conclusion, the aluminium cage seems the most viable solution for this rim drive.

4 Conclusion

This paper presents a feasibility study for a 250 kW induction motor rim drive to power a BLI fan for aircraft applications. The baseline design using 0.35 mm thick cobalt-iron laminations and aluminium rotor bars, achieved an efficiency of 96.4% for an active mass of only 19 kg. The aluminium rotor cage keeps the rotating mass to a minimum and is beneficial for the centrifugal stress induced in the rotor teeth. The high tensile-stress cobalt-iron laminations (VacodurS+) can withstand the centrifugal stress: only the aluminium rings need additional support banding, which can be accommodated easily onto the ring spigots. Replacing aluminium in the rotor cage with copper brings only a marginal efficiency improvement and causes a severe increase in the centrifugal stresses in the rotor, which cannot be withstood using available high-saturation lamination materials unless additional banding is put in place.
Efficiencies in excess of 97% can only be achieved using 0.1mm thick laminations in the stator in the baseline design with the aluminium rotor cage.

References

[1] Kim, H. D., Brown, G. V., Felder, J. L.. 'Distributed turboelectric propulsion for hybrid wing body aircraft', *9th International Powered Lift conference*, London, UK, 2008.

[2] Felder, J. L., Kim, H. D., Brown, G. V., & Chu, J. (2011, January). An examination of the effect of boundary layer ingestion on turboelectric distributed propulsion systems. In *49th AIAA aerospace sciences meeting including the new horizons forum and aerospace exposition* (pp. 2011-300).

[3] Kang, W., Zhang, J., Yang, L.: 'Research on Boundary Layer Ingestion effects of distributed propulsion configuration', *Proceedings of 2014 IEEE Chinese Guidance, Navigation and Control Conference*, Yantai, pp. 624-629, 2014.

[4] Gohardani, A. S., Doulgeris, G., Singh, R.: 'Challenges of future aircraft propulsion: A review of distributed propulsion technology and its potential applications for the all-electric commercial aircraft', *Progr, Aerosp. Sci.* vol. 47, (5), pp. 369-391, Jul. 2011.

[5] Berg F., Palmer J., Miller P., Husband M., Dodds G.: 'HTS Electrical System for a Distributed Propulsion Aircraft', *IEEE Transactions on Applied Superconductivity*, vol. 25, (3), pp. 1-5, June 2015.

[6] Tuohy, P.M., Smith, A.C., Husband, S.M., Hopewell, P.: 'Rim-drive marine thruster using a multiple-can induction motor', *IET Electr. Pow. Appl.*, vol. 7, (7), pp. 557-565, Aug. 2013.

[7] https://www.schottel.de/marine-propulsion/srt-rim-thruster

[8] J. Pyrhonen, T. Jokinen, V. Hrabvocova, 'Design of rotating electrical machines', *John Wiley & Sons*, 2008, pp. 259-261.

[9] http://www.vacuumschmelze.com/en/home.html

[10] https://cogent-power.com/downloads

[11] J. F. Gieras, J. Saari, 'Performance calculation for a high-speed solid-rotor induction motor', IEEE Trans. Ind Electron., vol 59, no. 6, pp. 2689-2700, June 2012.